

Photon counting, censor corrections, and lifetime imaging for improved detection in two-photon microscopy

Jonathan D. Driscoll, Andy Y. Shih, Satish Iyengar, Jeffrey J. Field, G. Allen White, Jeffrey A. Squier, Gert Cauwenberghs and David Kleinfeld

J Neurophysiol 105:3106-3113, 2011. First published 6 April 2011; doi:10.1152/jn.00649.2010

You might find this additional info useful...

Supplemental material for this article can be found at:

<http://jn.physiology.org/content/suppl/2011/04/07/jn.00649.2010.DC1.html>

This article cites 46 articles, 6 of which can be accessed free at:

<http://jn.physiology.org/content/105/6/3106.full.html#ref-list-1>

Updated information and services including high resolution figures, can be found at:

<http://jn.physiology.org/content/105/6/3106.full.html>

Additional material and information about *Journal of Neurophysiology* can be found at:

<http://www.the-aps.org/publications/jn>

This information is current as of June 16, 2011.

Photon counting, censor corrections, and lifetime imaging for improved detection in two-photon microscopy

Jonathan D. Driscoll,¹ Andy Y. Shih,¹ Satish Iyengar,² Jeffrey J. Field,^{1,3} G. Allen White,¹ Jeffrey A. Squier,³ Gert Cauwenberghs,^{4,5} and David Kleinfeld^{1,5}

¹Department of Physics, University of California at San Diego, La Jolla, California; ²Department of Statistics, University of Pittsburgh, Pittsburgh, Pennsylvania; ³Department of Physics, Colorado School of Mines, Golden, Colorado; and ⁴Department of Bioengineering and ⁵Section of Neurobiology, University of California at San Diego, La Jolla, California

Submitted 23 July 2010; accepted in final form 30 March 2011

Driscoll JD, Shih AY, Iyengar S, Field JJ, White GA, Squier JA, Cauwenberghs G, Kleinfeld D. Photon counting, censor corrections, and lifetime imaging for improved detection in two-photon microscopy. *J Neurophysiol* 105: 3106–3113, 2011. First published April 6, 2011; doi:10.1152/jn.00649.2010.—We present a high-speed photon counter for use with two-photon microscopy. Counting pulses of photocurrent, as opposed to analog integration, maximizes the signal-to-noise ratio so long as the uncertainty in the count does not exceed the gain-noise of the photodetector. Our system extends this improvement through an estimate of the count that corrects for the censored period after detection of an emission event. The same system can be rapidly reconfigured in software for fluorescence lifetime imaging, which we illustrate by distinguishing between two spectrally similar fluorophores in an in vivo model of microstroke.

fluorescence imaging microscopy; noise; photon pile up

TWO-PHOTON LASER SCANNING MICROSCOPY (TPLSM) (Denk and Svoboda 1997; Denk et al. 1990, 1995; Helmchen and Denk 2005; Yasuda et al. 2006) involves the periodic excitation of molecules by hundred-femtosecond laser pulses, followed by the emission of fluorescent light before the arrival of the next pulse. Despite the relatively large number of photons in each excitation pulse, roughly 100 million at the focus of the objective for nonsaturating intensities, the average number of fluorescence photons that are detected is typically of order one or less (Neher and Hopt 2001; Tsai and Kleinfeld 2009). Thus it is imperative to optimize all aspects of TPLSM, from ensuring that the excitation beam is free from temporal and spatial aberrations (Cui 2011; Field et al. 2010b; Ji et al., 2010; Rueckel et al. 2006; Tsai et al. 2007) to the collection and detection of as many of the emitted photons as possible (Engelbrecht et al. 2008).

All measurements of light contain shot noise, which reflects the discrete nature of photons and limits the signal-to-noise ratio (SNR) for a pixel with an average count of N photons to $\text{SNR} = \sqrt{N}$. Ideally, the photodetection process will not add to this noise. Photomultiplier tubes (PMTs) are universally used to convert the arrival of a photon into a pulse of current, which is then amplified, filtered or integrated, and digitized to generate a pattern of the intensity of fluorescent emission as a function of the position of the focus of the excitation beam. This pattern forms the optically sectioned planar image reported with TPLSM (Denk et al. 1990). Photomultiplier tubes

offer a unique combination of good quantum efficiency, high conversion gain, high speed, and linearity of the output current with incident intensity. However, the serial amplification of photocurrents along the dynode chain in a PMT results in a variation in the amplitude of the individual output pulses (Zworykin et al. 1936) that multiplies the variance of the shot effect (Shockley and Pierce 1938). The exact value of this additional noise depends on details of the PMT but is typically 20–70%.

Photon counting is commonly used as a means to circumvent variation in the intensity of the output pulses from the PMT. This technique is based on the assumption that current pulses that exceed a threshold amplitude are the result of photoelectrons generated by absorption of a single photon at the cathode of the PMT, as opposed to a thermally generated electrons. Photon counting devices employ a discriminator to convert analog pulses from the PMT into digital pulses, which are then summed. Since each photon will result in exactly one count, this eliminates a source of variability in the detection process.

Photon counting is preferred so long as the rate of emitted photons is low, so that each emitted photon is counted before a second photon arrives. Although the chance of two photons arriving at the PMT at exactly the same instance is nil, dispersion of the electron current in the PMT, the capacitance of cables, and the response time of amplifiers leads to a photocurrent pulse with a width of one to a few nanoseconds. This creates a censored period after a photon arrives that briefly blocks the counting of subsequent photons. Uncertainty in the number of uncounted events constitutes a source of variability. This uncertainty is negligible when the rate of fluorescent emission is low but will exceed the variability associated with the amplitude of the photocurrent pulses when the rate of emission is high. The best SNR is thus obtained by switching from photon counting to analog integration when the dominant noise source changes from analog variability to uncertainty in the count. However, algorithms to estimate the number of missed counts, as well as to identify the exact count at which the switch from counting to analog detection should occur, do not appear in past literature.

In this report we describe a reconfigurable photon counting system that achieves a resolution of 3.2 ns between successive pulses with a temporal accuracy of 1.5 ns per photon. It is used in conjunction with a maximum likelihood estimate of the number of censored pulses as a means to increase the dynamic range of counting. At the core of the system is a high-speed complex programmable logic device (CPLD) that operates

Address for reprint requests and other correspondence: D. Kleinfeld, Dept. of Physics 0374, Univ. of California, 9500 Gilman Drive, La Jolla, CA 92093-0374 (e-mail: dk@physics.ucsd.edu).

together with commercially available components to transfer pulses to a master computer at the typical 0.5- to 2.5-MHz rates of pixel acquisition. Although photon counting has been previously utilized for TPLSM (Amir et al. 2007; Benninger et al. 2008; Buehler et al. 2005; Field et al. 2010b; Sheetz et al. 2008; Vucinic and Sejnowski 2007), previous systems did not transfer the measured counts at these clock rates. Furthermore, the flexibility of our counter allows it to be rapidly reconfigured for fluorescent lifetime imaging (FLIM) (Berezin and Achilefu 2010; Harvey et al. 2008; Konig et al. 1996; Pepperkok et al. 1999; Yasuda et al. 2006) and potentially other modes of nonlinear imaging.

METHODS

Optomechanics. All data were obtained with a custom-built two-photon microscope, as described previously (Tsai and Kleinfeld 2009), and a tunable Ti:Al₂O₃ pulsed laser (Mira 900; Coherent) that operated at 75.5 MHz. We used $\times 20$, 1.0 numeric aperture (NA) (Zeiss) and $\times 40$, 0.8 NA (Olympus) dipping objectives. The microscope was controlled with MPScope 2.0 software (Nguyen et al. 2006, 2009), which synchronized data acquisition, both analog and digital, with bidirectional scanning of galvanometric mirrors.

Electronics. Signal acquisition begins with a PMT (H7422-40; Hamamatsu) that converts photons into brief current pulses with a conversion gain of $\sim 3 \times 10^5$. For imaging by analog integration, the PMT output is switched (ZSWA-4-30DR; Mini-Circuits) to a current-to-voltage converter and a direct current-coupled amplifier, both with a 0.3- μ s time constant, low-pass filtered with a 3-pole Bessel filter (model 3202; Kronhn-Hite) set so that the -3 -dB cutoff frequency of the filter, denoted f_c , is equal to $\sqrt{\ln(2)}/\pi f_{\text{pixel}}$, where f_{pixel} is the frequency of the pixel clock (Tan et al. 1999), and then digitized by an analog-to-digital board (PCI-6110; National Instruments), where it is sampled at the pixel clock rate (Fig. 1).

For imaging by photon counting, the output of the PMT is directed through a high-speed alternating current-coupled amplifier (ZPUL-

30P; Mini-Circuits), and the signal is converted to a transistor-to-transistor logic (TTL) pulse with a discriminator, either a commercial device (PRL-350TTL; Pulse Research Lab) or one of local design (Fig. S1 in Supplementary Information on Firmware and Hardware). (Supplemental material for this article is available online at the *Journal of Neurophysiology* website.) The threshold is set above the thermal voltage noise and typically at 0.2 times the measure height of the current pulse. All lines are terminated at 50 Ω . The TTL pulses are counted using a custom photon counting board, implemented with a CPLD (ispMach LC4256V; Lattice). The counts are read from the board at the pixel clock rate by a digital interface board (DIO-32HS, National Instruments) on a Windows-based computer. The firmware for the CPLD is written in ispLevel Classic (Lattice Semiconductor) and is flashed to the CPLD board through a standard parallel port interface. The CPLD implements a high-speed dual ripple counter (Fig. S2 in Supplementary Information on Firmware and Hardware), in which the active counter alternates at each imaging pixel. This allows time for the counters to settle before being read by the computer interface board, which inputs 32 bits in parallel from the CPLD counters at the pixel clock rate.

For FLIM, a timing signal from the laser excitation pulse must be passed to the CPLD counting board. We split a small portion of the pulsed laser excitation light onto a high-speed photodiode (DET10A; Thor Labs). This signal is amplified (ZJL-4G+; Mini-Circuits) and divided by a passive coupling device (ZFDC-10-5; Mini-Circuits). The larger portion of the signal is piped to a discriminator, where it is converted to a TTL logic level signal, while the weaker signal is directed to an oscilloscope to monitor the mode-locking of the excitation laser. Fluorescence lifetime data for each pixel are acquired by sequentially enabling a series of six separate counters on the CPLD device. These counters are gated so that the first counter is enabled for 0–1.5 ns after the initial laser excitation pulse, the second counter is enabled for 1.5–3 ns after the laser excitation pulse, and so forth. The end result is a six-bin histogram of arrival times for fluorescence photons from which the exponential decay time of the fluorophore, τ , can be calculated. The implementation of multiple counters for FLIM, acquisition of specific number of counts per pixel clock, and

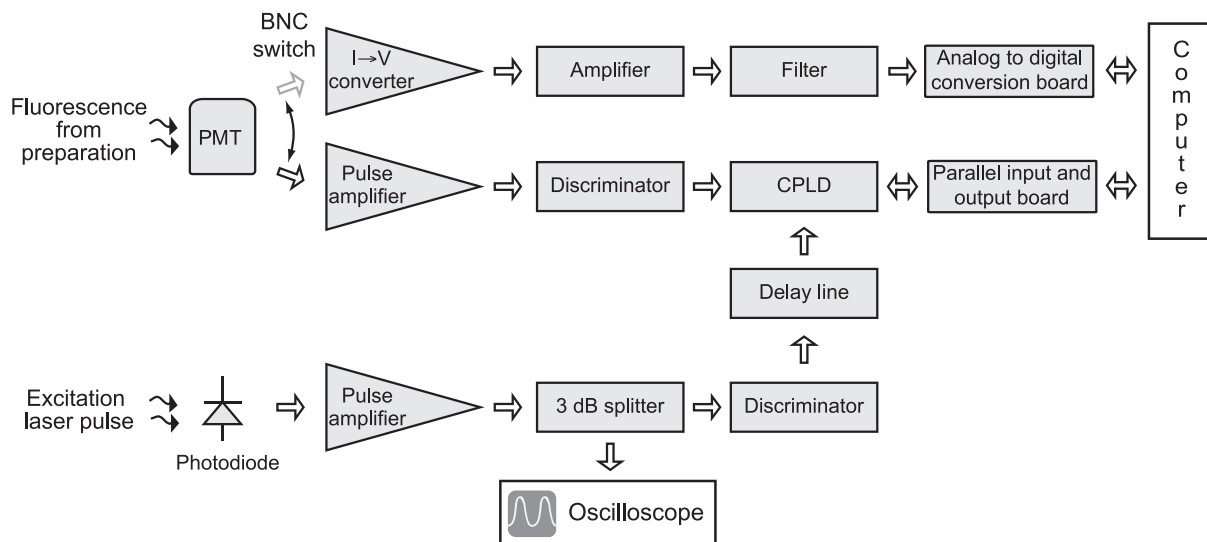


Fig. 1. Photon counting system. Single photons arriving at the photomultiplier tube (PMT) are converted to discrete current pulses. For analog integration, the signal is routed to a custom-built direct current-coupled amplifier, filtered using a Bessel filter, and passed to the analog input of the data acquisition card. For photon counting, the signal from the PMT is sent to a wide-band amplifier and then into a discriminator to convert the pulses to a transistor-to-transistor logic (TTL)-level logic signal. These pulses are read by a custom-built board containing a complex programmable logic device (CPLD), which implements a dual counter scheme for each channel and sends the output to a digital interface card on the computer. In addition, a portion of the laser excitation beam is split off with a glass slide and sent to a high-speed photodiode. The output from the diode is amplified with a high-speed amplifier and split into 2 signals using a passive transformer-based splitter. One of the outputs from the coupler is sent to an oscilloscope, and the other is converted to TTL-level pulses with an additional discriminator channel, sent through an adjustable fine-scale analog delay line, and routed to the CPLD for use with fluorescence lifetime imaging microscopy (FLIM). *I*→*V* converter, current-to-voltage converter; BNC, Bayonet Neill-Concelman connector.

simultaneous data acquisition by two or more PMTs is detailed in Supplementary Information on Firmware and Hardware and Figs. S2–S4.

The timing signal for the laser excitation pulse must be aligned to coincide with the start of the fluorescence excitation. We thus delay the signal from the excitation pulse to maximize fluorescence counts acquired in the first time bin. A coarse delay line, with a resolution of 1.5 ns, is implemented in the firmware of the CPLD (Fig. S3A in Supplementary Information on Firmware and Hardware). A fine-grained delay is achieved with a custom analog delay line that was constructed by switching among 12 lengths of impedance-matched (50 Ω) wire that incremented the delay from 0 to 1.65 ns in increments of 0.15 ns.

In vivo physiology. Our subjects were C57Bl6 mice and green fluorescent protein-expressing inhibitory interneuron (GIN) mice that ranged in mass from 20 to 30 g. All procedures were performed in anesthetized animals. Anesthesia was induced with 4% (vol/vol) isoflurane in 30% oxygen and 70% nitrous oxide and was maintained with 1–2% (vol/vol) isoflurane. The care and experimental manipulation of our mice were reviewed and approved by the Institutional Animal Care and Use Committee at the University of California at San Diego.

In the GIN animals, a craniotomy was performed to generate a cranial window with the dura left intact (Helmchen and Kleinfeld 2008; Holtmaat et al. 2009). Individual neurons were imaged as described (Drew et al. 2010). The C57Bl6 mice were used to form occlusions to single penetrating arterioles, as described previously (Blinder et al. 2010; Nishimura et al. 2007), with some modifications for mice. The pial vasculature was imaged through a thinned skull preparation reinforced with a glass coverslip (Drew et al. 2010). The vasculature was labeled by injecting 50 μl of 2.5% (wt/vol) Texas red-dextran (70 kDa; Invitrogen) in phosphate-buffered saline (PBS) through the infraorbital vein. Targeted photothrombosis was initiated by illuminating a target vessel with focused 530-nm laser light immediately following the injection of 50 μl of 1.25% (wt/vol) rose Bengal in PBS, also administered through the infraorbital vein. After confirmation of single vessel occlusion, the mice were allowed to survive for 2 days before reimaging. The vasculature was relabeled with another injection of Texas red-dextran. The nuclei of dying, membrane-disrupted cells were labeled by a single intraperitoneal injection of 1 mg/kg propidium iodide in PBS, as described previously (Unal Cevik and Dalkara 2003).

Immunohistology. Mice were injected with a fatal dose of pentobarbital and transcardially perfused with PBS followed by 4% (wt/vol) paraformaldehyde in PBS. The brains were removed and cryoprotected in 30% (wt/vol) sucrose overnight. The forebrain was cryosectioned coronally at a thickness of 50 μm, and immunohistochemistry was performed on free-floating sections. Tissues were stained with primary antibodies for microtubule-associated protein-2 (MAP-2; no. AB5622, Chemicon) and secondary anti-rabbit Alexa 488 antibodies. Images were obtained using a Fluoview 1000 confocal microscope with an oil-immersion ×63 objective.

RESULTS

At low signal intensities, the average fluorescence that follows each laser pulse will contain, on average, significantly less than one photon. The signal must be integrated across multiple pulses, and the background electronic noise from the PMT, as well as from associated analog electronics, will reduce the ability to distinguish image features from the background. As an example, we used *in vivo* TPLSM (Svoboda et al. 1997) to image neurons in parietal cortex of mice that express green fluorescent protein in somatostatin-positive inhibitory cells (Bozza et al. 2004). The same field was imaged, using the same

rate for the pixel clock, with our photon counting scheme (Fig. 2A) and with traditional analog integration (Fig. 2B). In general, the lower noise in the counting image reveals processes and details that are not seen in the analog images ($n = 5$ fields). A histogram of the counts and normalized intensity shows a clearly perceptible hump in the digital count (star in Fig. 2C), consistent with a non-Poisson distribution of the signal photons.

The scaling of excess noise with analog integration versus photon counting was directly tested by obtaining equivalent images of a sample, fluorescein-labeled cellulose that had a broad spatial distribution of emission intensities (Fig. 2, D and E). The mean count per pixel is βr , where r is the number of laser pulses in the period of the pixel clock, i.e., $r \equiv \int_{\text{pulses}} f_{\text{pixel}} \sim 100$, and β is the measured number of emissions per laser pulse (Table 1). The variance for the photon counting data, denoted σ^2 , scales identically with the mean count per pixel, i.e., $\sigma^2 = \beta r$. In contrast, the analog signal showed excess variance compared with the Poisson limit (Fig. 2F). The data were well described by the phenomenological fit of $\sigma^2 = (1 + \eta)\beta r$, with $\eta = 0.57$ for our conditions.

Correction to the photon count and variance. We analyzed the effect of near-simultaneous arrival of multiple photons, or photon pileup (Coates 1968), that can occur when the lifetime of the fluorophore is comparable to the time resolution of the detection electronics. This is the typical case with genetically expressible indicators and most biologically relevant organic dyes, but not for quantum dots (Berezin and Achilefu 2010; Shaner et al. 2005). At modest to high imaging intensities, a single laser excitation pulse can result in two or more signal photons arriving at the PMT within the pulse-pair resolution of a single channel of the photon counter, denoted Δ , where $\Delta = 3.2$ ns for our system. Thus pairs or n -tuples of photons are counted as a single event, because all but the first photon are censored for a period Δ . This phenomenon leads to the loss of information as to the exact number signal photons per laser excitation pulse.

How can we estimate the true count, α , from the measured count, β ? In principle, there is a monotonic relation between these quantities. However, as an approximation, one can estimate α from the measured distribution of counts with zero, one, two, etc., photons per laser pulse. We consider first the case of using only the number of samples with zero events, i.e., laser pulses that did not lead to a photocurrent, denoted r_0 . A maximum likelihood estimate (MLE) yields an estimate, denoted $\hat{\alpha}$, in closed form (Supplementary Information on Count Estimate), i.e.,

$$\hat{\alpha} = -\ln(r_0/r) \tag{1}$$

and

$$\sigma^2 = \frac{r - r_0}{r \cdot r_0} \tag{2}$$

The value of $\hat{\alpha}$ for each pixel forms the image, and the ratio $\hat{\alpha}/\sigma$ forms the MLE of the SNR for that pixel.

An improved MLE for $\hat{\alpha}$ is formed by including r_1 , the number of laser pulses that lead to exactly one measured count. This calculation incorporates the possibility that additional photons may have arrived in the censored period and yields an expression for $\hat{\alpha}$ that must be evaluated numerically (Supple-

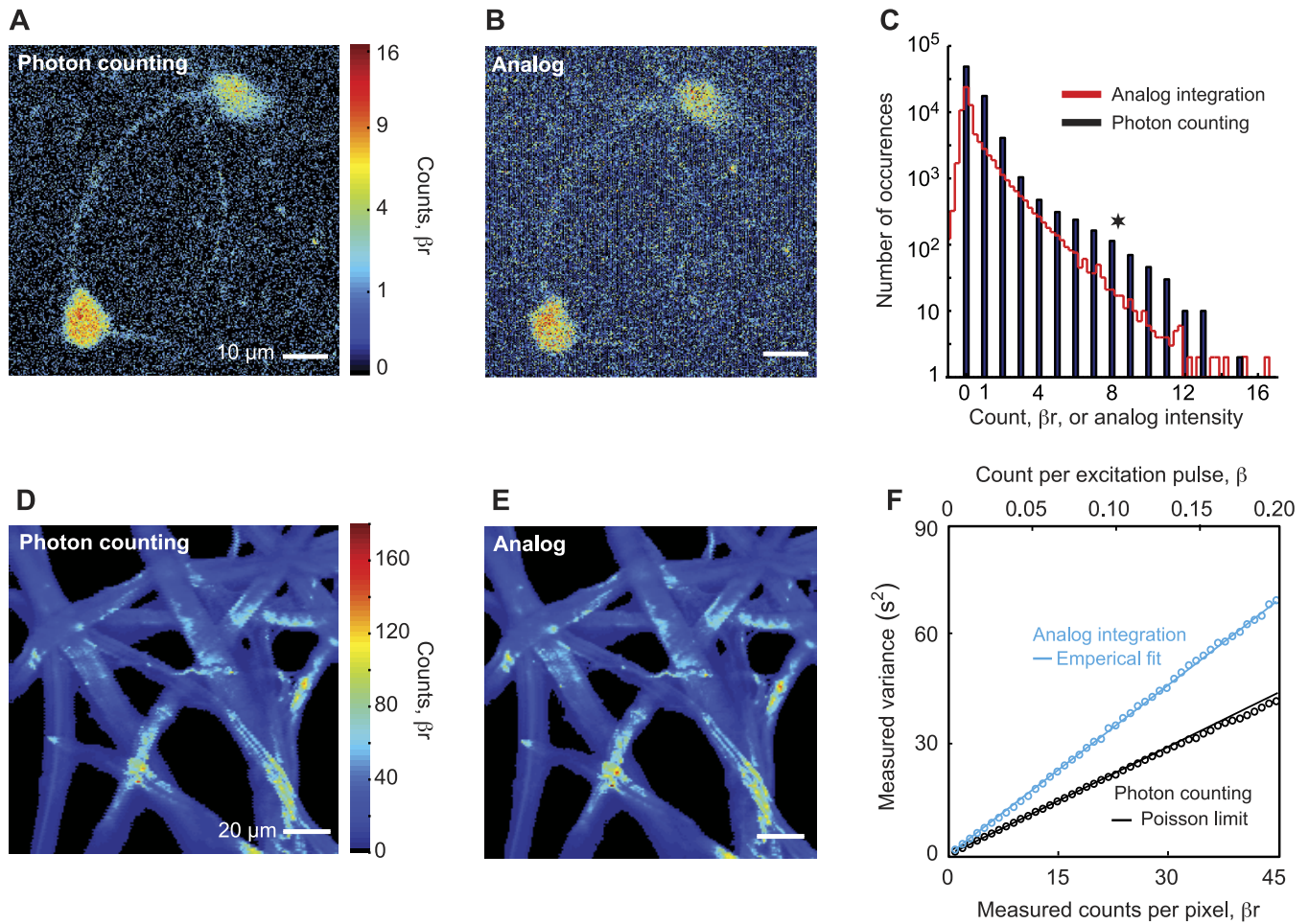


Fig. 2. Comparison of digital and analog images under conditions of low emission rates. *A*: photon counting image of labeled neurons in a green fluorescent protein-expressing inhibitory interneuron (GIN) mouse at low signal level: single frame, pixel clock of $5 \mu\text{s}$ ($r = 383$ laser pulses per pixel), $\sim 125 \mu\text{m}$ below the pia, and $\sim 30 \text{ mW}$ of incident laser power as measured through the objective at $\lambda = 900 \text{ nm}$. *B*: image of the same field in *A* taken via analog integration using the same pixel clock. For comparison of the analog and digital images, the baseline amplitude has been subtracted from the analog image and the mean value of the intensity scaled to match the mean values from the photon counting data. Note that the fine processes are barely visible compared with the digital image in *A*. *C*: histogram for the images in *A* and *B* using a binwidth of 0.25 counts. Only discrete values, i.e., 0, 1, 2, . . . , are recorded with photon counting. The star indicates excess counts that correspond to signal photons. *D*: photon counting image of cellulose stained with rhodamine B at low signal level: 200-frame average, pixel clock of $3 \mu\text{s}$ ($r = 230$), and $\sim 6 \text{ mW}$ of incident laser power at $\lambda = 800 \text{ nm}$. *E*: image of the same field in *D* taken via analog integration using the same frame averaging and pixel clock. *F*: plot of the variance for the photon counting data, with the Poisson fit of $\sigma^2 = \beta r$, along with the variance for the analog data with a phenomenological fit of $\sigma^2 = 1.57 \beta r$.

mentary Information of Count Estimate). We use the Newton-Raphson method to find the value of α that maximizes the log-likelihood function $l(\alpha)$, where

$$l(\alpha) = r_0 \ln[p_0(\alpha)] + r_1 \ln[p_1(\alpha)] + (r - r_0 - r_1) \ln[1 - p_0(\alpha) - p_1(\alpha)] \quad (3)$$

with

$$p_0(\alpha) = e^{-\alpha} \quad (4)$$

and

$$p_1(\alpha) = \frac{e^{-\alpha e^{-\Delta\tau}} - e^{-\alpha}}{1 - e^{-\Delta\tau}}. \quad (5)$$

The variance is found by numerically computing the second derivative of $l(\alpha)$ with respect to α , evaluated at $\alpha = \hat{\alpha}$ (Eq. 3) so that

$$\sigma^2 = - \left(\frac{\partial^2 l(\alpha)}{\partial \alpha^2} \Big|_{\alpha=\hat{\alpha}} \right)^{-1}. \quad (6)$$

Note that the above expressions (Eqs. 1–6) can further include corrections for emissions that fail to occur with the time between laser pulses (Supplementary Information on Count Estimate). These emissions are not lost but can be counted as originating from a subsequent laser pulse.

We applied the above relations to images taken under relatively high laser intensities, for which the average count per laser pulse was well above one for bright regions of the image. We compared the image found with uncorrected counts (Fig. 3*A*), the image and SNR using the estimate of $\hat{\alpha}$ at each pixel with just the number of pulses with no detected emission (Fig. 3*B1* using Eq. 1 and Fig. 3*B2* using Eq. 2), the image and SNR using the estimate of $\hat{\alpha}$ at each pixel with both the number of pulses with zero and exactly one detected emission (Fig. 3*C1* using Eqs. 3–5 and Fig. 3*C2* using Eq. 6), and, last, the image

Table 1. Symbols used in analysis of measured counts

Symbol	Definition	Typical Value
f_{pulses}	Frequency of laser pulses	75.5 MHz
f_{pixel}	Frequency of pixel clock	0.5–2.5 MHz
τ	Fluorescent lifetime of dye	~4 ns for fluorescein
Δ	Censored period or pulse-pair resolution	3.1 ns
α	True, mean number of photon counts per laser pulse	<3
β	Measured, mean number of photon counts per laser pulse	
$\hat{\alpha}$	MLE number of photon counts per laser pulse	
r	Sample size or laser pulses per pixel clock, $f_{\text{pulses}}/f_{\text{pixel}}$	30–150
r_0	Number of samples with a count of zero per laser pulse	
r_1	Number of samples with a count of exactly one per pulse	

MLE, maximum likelihood estimate.

obtained with analog detection (Fig. 3, *D1* and *D2*). These data illustrate three key points. First, the dynamic range of the uncorrected image was compressed compared with the corrected images (cf. *A* with *B1* and *C1* in Fig. 3) and compared with the analog image (cf. *A* with *D1* in Fig. 3). This occurs from the systematic loss of counts the high emission rates associated with bright pixels. Second, the SNR increases substantially when both r_1 and r_0 are used to estimate $\hat{\alpha}$ for each pixel, compared with just r_0 (cf. *B2* with *C2* in Fig. 3). Last, the SNR when both r_1 and r_0 are used to estimate $\hat{\alpha}$ for each pixel approaches that of analog recording at these high light levels, for which there is substantial censoring.

Crossover from photon counting to analog integration. At lower imaging intensities, photon counting offers an improved SNR compared with analog integration (Figs. 2*F* and 3*E*). At high intensities, however, the uncounted photons in

the censored region result in additional variance that degrades the SNR of photon counting. There is a “crossover” point, above which analog integration yields a higher SNR for bright pixels and is preferable. In the example of Fig. 3, obtained with relatively high incident intensity, the crossover point is $\hat{\alpha} = 0.8$ when only the number count for no emissions is used, but $\hat{\alpha} = 1.5$ when both the number of events with zero count and one count are used (Fig. 3*E*). There is a 0.45 chance of emitting two or more photons per laser pulse at the intensity that corresponds to $\hat{\alpha} = 1.5$, clearly demonstrating the utility of our approach to correct for censored counts.

In vivo detection of neuronal cell death using FLIM. The distribution of time between an excitation pulse and the returned fluorescence photon is a means to determine the lifetime of the fluorophores (de Grauw and Gerritsen 2001; Suhling et al. 2005; Wang et al. 1990). Thus FLIM can be exploited to separate multiple fluorophores with overlapping emission spectra but different fluorescence lifetimes within the same biological sample (Steinkamp et al. 1999). We use FLIM to distinguish between two red emission dyes, Texas-red dextran and propidium iodide, in a model of microstrokes in which single penetrating arterioles are blocked by targeted photoexcitation (Blinder et al. 2010; Nishimura et al. 2007). The single occlusion leads to a cessation of blood flow in a 500- μm -diameter neighborhood of the block and the eventual formation of a cyst. Both dyes are essential to the assessment of neuronal damage. Texas red-dextran enables deeper vascular labeling than related molecules with green emission, such as fluorescein-dextran, and is used to locate the margin of the stroke. Propidium iodide is commonly used as a cell death indicator, because it preferentially stain cells with membranes disrupted by necrosis or apoptosis. Past studies have shown that propidium iodide can be used as a histological assay of cell damage when administered as an intravenous injection (Unal Cevik and Dalkara

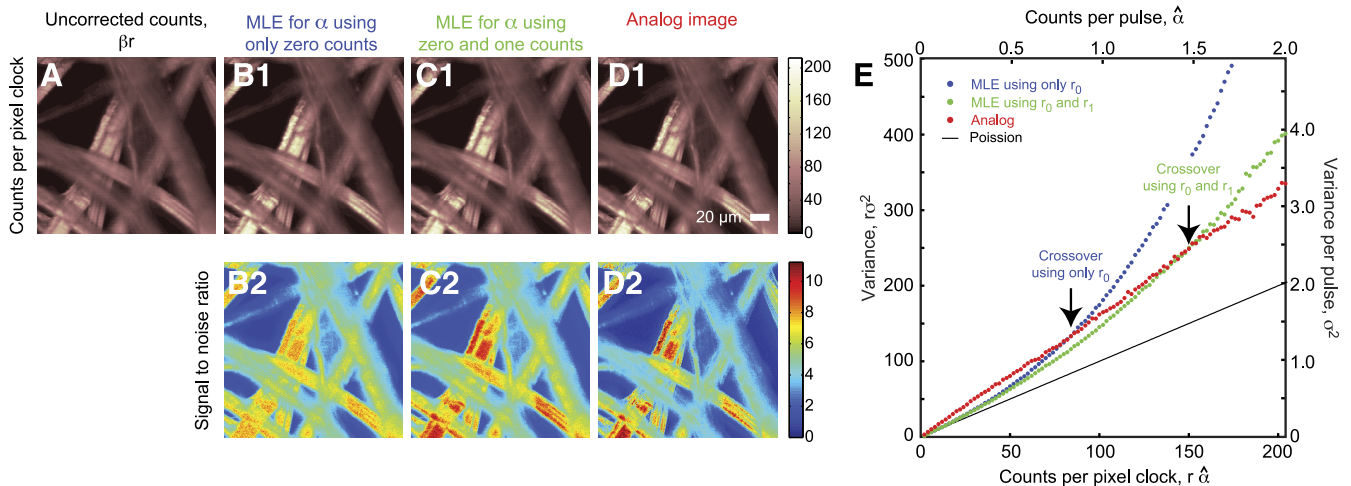


Fig. 3. Measured and estimated true photon counts and signal-to-noise ratios (SNR) for imaging under conditions of high emission rates. The image is cellulose paper stained with rhodamine 6G, for which τ , the exponential decay time of the fluorophore, is 4.1 ns. We used a pixel clock of 1.35 μs ($r = 102$) and 5.6 mW of incident laser power, with $\lambda = 840$ nm. We averaged 200 frames per image. *A*: plot of frame-averaged intensity, βr , for the raw counts. *B*: the image (*B1*) and SNR (*B2*) calculated from the number of samples with zero counts (Eqs. 1 and 2) on a pixel-by-pixel basis. *C*: the image (*C1*) and SNR (*C2*) calculated from the number of samples with both zero and one count (Eqs. 3–6) on a pixel-by-pixel basis. *D*: the image formed using analog integration with a low-pass filter frequency of 448 kHz (*D1*) and the SNR found by direct calculation of the frame-to-frame variability for each pixel (*D2*). The data were scaled so that the intensity of the averaged analog image matched that of the corrected digital image. *E*: plot of the variance as a function of the counts using data similar to that in *B1*, *C1*, and *D1*, but with an excitation power of 7.0 mW to increase the emission rate by 55%. The arrows mark the number of counts per pixel where analog integration will have a lower noise than photon counting together with the maximum likelihood estimate (MLE) for $\hat{\alpha}$.

2003). We now extend this technique to image cell death in vivo.

Two-photon imaging based solely on intensity, or counts, yields individually labeled cells and vessels that are indistinguishable on the basis of brightness (Fig. 4A). Imaging based on lifetime clearly distinguishes between the two structures (Fig. 4B), consistent with the 4.1-ns lifetime of Texas red (Brismar et al. 1995) and the 6- to 12-ns lifetime of propidium iodide when bound to DNA (Hanley et al. 2002). The merged counts and lifetime clearly highlights dying cells (red cells; arrowhead in Fig. 4C) and filled microvasculature (blue vessel; arrow in Fig. 4C). Post hoc histological analysis of this region shows that propidium iodide-labeled neurons are most prominent within the border of the microinfarction (Fig. 4D) and that labeled cells appear to be primarily neurons, based on immunohistochemistry with the pan-neuronal marker MAP-2 (Fig. 4E).

DISCUSSION

Photon counting (Fig. 1) provides a simple way of increasing the SNR of images obtained with two-photon microscopy for low and medium imaging intensities (Fig. 2). At higher intensities, the increased SNR is offset by the arrival of multiple photons per laser pulse. The undercounting inherent in this process results in an additional noise source. Our analysis shows how to correct for undercounting in a manner that essentially doubles the count at which one needs to switch to analog integration (Eqs. 3–6). In fact, the correction for cen-

sored counts is sufficiently good to obviate the need for analog detection, even at high emission rates (Fig. 3).

Theoretical analysis of the shot-to-shot variation in output pulses from the PMT predicts that the analog signal should have a multiplicative factor of $\eta = (1 - g^{-d+1})/(g - 1)$ excess noise power over the Poisson limit (Shockley and Pierce 1938), where g is the gain per stage in the PMT at a particular supply voltage and d is the number of stages. For $g = 3.5$ and $d = 9$, parameters for the operating point of our PMT in these studies, the theoretical value of $\eta = 0.4$ falls short of the observed value of $\eta = 0.6$. The reason for this excess is unclear, yet the implication is that photon counting is effective at higher intensities than suggested by theory.

Our system allows for uninterrupted counting at speeds up to 350 MHz with the use of relatively inexpensive commercially available parts. In addition, by creating the electronics around a reprogrammable CPLD core and by locking the counters to the onset of the excitation pulse, we are able to extend the photon counting device to acquire fluorescence lifetime images with 1.5-ns binwidths (Fig. 4). Locking of the counters to the laser pulse is also essential when alternate pulses are used to acquire different modalities, such as switching between focal depth or polarization (Carriles et al. 2009; Field et al. 2010a). Other potentially useful configurations are possible with only a change in firmware, such as gating to isolate the extremely short-lived signals that are generated by second (Campagnola et al. 2001; Moreaux et al. 2000) and third (Débarre et al. 2006; Squier et al. 1998)

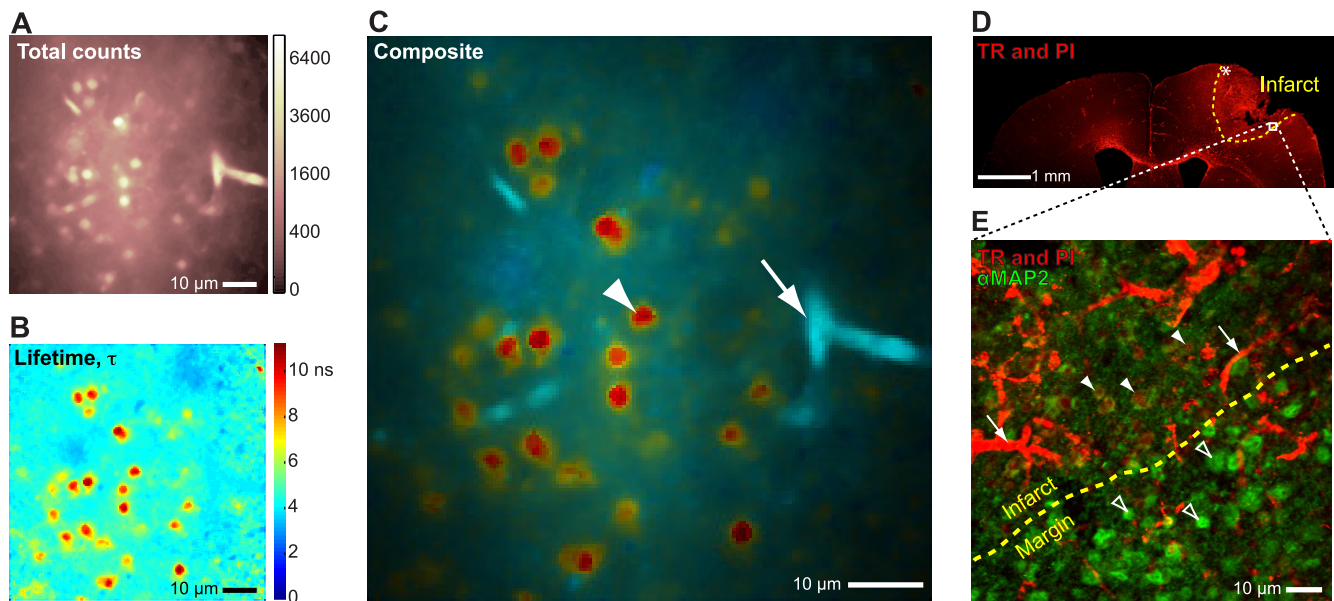


Fig. 4. Fluorescence intensity and lifetime imaging of spectrally similar dyes in a mouse model for experimental stroke. *A*: an intensity image collected with in vivo two-photon laser scanning microscopy (TPLSM) within infarcted tissue shows propidium iodide (PI)-labeled cells and Texas red-dextran (TR)-labeled vessels, which are indistinguishable by intensity alone. Images were acquired 140 μm below the pia, using 30 mW of incident laser power, at $\lambda = 825$ nm. Images were acquired at 512×512 resolution and then binned 3×3 for analysis and median filtered. We averaged 132 frames with $r = 68$ laser pulses per pixel. *B*: a fluorescence lifetime image demonstrating that labeled vessels and the cells can be distinguished on the basis of lifetime of the different fluorophores. *C*: a combined fluorescence lifetime and intensity image, with the color indicating lifetime and the saturation indicating number of photon counts, enables vessels (arrow) and cells (arrowhead) to be clearly distinguished. *D*: coronal section showing infarcted cortical region 2 days following occlusion of a single penetrating arteriole. Note that extravasation of the TR dye and PI labeling of necrotic cells is prominent within the infarct. An asterisk labels the approximate location of in vivo imaging. *E*: magnified view of the infarct in *D* showing strong microtubule-associated protein-2 (MAP-2) staining (green) of viable neurons within the stroke margin (open arrowheads). Within the stroke, intensity of MAP-2 labeling decreases and damaged neurons exhibit PI labeling of nuclei (arrowheads). Extravasation of TR (arrows) is more prominent within the infarcted region.

harmonic process and coherent anti-Stokes Raman scattering (Ly et al. 2007).

Continuing advances in high-speed digital electronics and serial communication suggest that a next-generation photon counting system may make use of a field-programmable gate array with a USB 2.0 serial communication channel, rather than the current CPLD and parallel communication channel. Furthermore, advances in PMT design and high-speed signal conditioning should decrease the censored period below 3 ns.

ACKNOWLEDGMENTS

We thank Earl M. Dolnick for involvement in the design of an analog integrator that predated this work, Quoc-Thang Nguyen for coding the first interface of MPScope with the photon counting device, Jing W. Wang for involvement in exploratory experiments, and Philbert S. Tsai for comments on the original manuscript, particularly with regard to the issue of censored counts.

The CPLD interface, as well as a variable time-delay and discriminator circuit, were developed by the University of California at San Diego (UCSD) Physics Electronic Shop. Confocal microscopy made use of the UCSD Cellular and Molecular Medicine Microscopy Shared Facility.

GRANTS

This work was supported by National Institutes of Health Grants AG029681 (to G. Cauwenberghs), EB003832 (to D. Kleinfeld and J. A. Squier), and OD006831 and RR021907 (to D. Kleinfeld) and National Science Foundation Grant DBI 0455027 (to D. Kleinfeld).

DISCLOSURES

No conflicts of interest, financial or otherwise, are declared by the author(s).

REFERENCES

- Amir W, Carriles R, Hoover E, Planchon TA, Durfee CG, Squier JA. Simultaneous imaging of multiple focal planes using a two-photon scanning microscope. *Opt Lett* 32: 1731–1733, 2007.
- Benninger KP, Ashby WJ, Ring EA, Piston DW. Single-photon-counting detector for increased sensitivity in two-photon laser scanning microscopy. *Opt Lett* 33: 2894–2897, 2008.
- Berezin MY, Achilefu S. Fluorescence lifetime measurements, and biological imaging. *Chem Rev* 110: 2641–2684, 2010.
- Blinder P, Shih AY, Rafie CA, Kleinfeld D. Topological basis for the robust distribution of blood to rodent neocortex. *Proc Natl Acad Sci USA* 107: 12670–12675, 2010.
- Bozza T, McGann JP, Mombaerts P, Wachowiak M. In vivo imaging of neuronal activity by targeted expression of a genetically encoded probe in the mouse. *Neuron* 42: 9–21, 2004.
- Brismar H, Trepte O, Ulfhake B. Spectra, and fluorescence lifetimes of lissamine rhodamine, tetramethylrhodamine isothiocyanate, Texas red, and cyanine 3.18 fluorophores: influences of some environmental factors recorded with a confocal laser scanning microscope. *J Histochem Cytochem* 43: 699–707, 1995.
- Buehler C, Kim KH, Greuter U, Schlumpf N, So PT. Single-photon counting multicolor multiphoton fluorescence microscope. *J Fluorescence* 15: 42–51, 2005.
- Campagnola PJ, Clark HA, Mohler WA, Lewis A, Loew LM. Second-harmonic imaging microscopy of living cells. *J Biomed Opt* 6: 277–286, 2001.
- Carriles R, Schafer DN, Sheetz KE, Field JJ, Cisek R, Barzda V, Squier JA. Imaging techniques for harmonic, and multiphoton absorption fluorescence microscopy. *Rev Sci Instrum* 80: 81101–81123, 2009.
- Coates PB. The correction for photon 'pile-up' in the measurement of radiative lifetimes. *J Sci Instrum* 1: 878–879, 1968.
- Cui M. A high speed wavefront determination method based on spatial frequency modulations for focusing through random scattering media. *Opt Express* 19: 2989–2995, 2011.
- de Grauw CJ, Gerritsen HC. Multiple time-gate module for fluorescence lifetime imaging. *Appl Spectrosc* 55: 670–678, 2001.
- Débarre D, Supatto W, Pena AM, Fabre A, Tordjmann T, Combettes L, Schanne-Klein MC, Beaurepaire E. Imaging lipid bodies in cells, and tissues using third-harmonic generation microscopy. *Nat Methods* 3: 47–53, 2006.
- Denk W, Piston DW, Webb W. Two-photon molecular excitation in laser-scanning microscopy. In: *Handbook of Biological Confocal Microscopy*, edited by Pawley JW. New York: Plenum, 1995, p. 445–458.
- Denk W, Strickler JH, Webb WW. Two-photon laser scanning fluorescence microscopy. *Science* 248: 73–76, 1990.
- Denk W, Svoboda K. Photon upmanship: Why multiphoton imaging is more than a gimmick. *Neuron* 18: 351–357, 1997.
- Drew PJ, Shih AY, Driscoll JD, Knutsen PM, Davalos D, Blinder P, Akassoglou K, Tsai PS, Kleinfeld D. Chronic optical access through a polished, and reinforced thinned skull. *Nat Methods* 7: 981–984, 2010.
- Engelbrecht CJ, Johnston RS, Seibel EJ, Helmchen F. Ultra-compact fiber-optic two-photon microscope for functional fluorescence imaging in vivo. *Opt Express* 16: 5556–5564, 2008.
- Field JJ, Carriles R, Sheetz KE, Hoover EE, Chandler EV, Tillo S, Hughes TE, Sylvester AW, Kleinfeld D, Squier JA. Optimizing the fluorescent yield in two-photon laser scanning microscopy with dispersion compensation. *Opt Express* 18: 13661–13672, 2010b.
- Field JJ, Sheetz KE, Chandler EV, Hoover EE, Young MD, Ding SY, Sylvester AW, Kleinfeld D, Squier JA. Differential multiphoton laser-scanning microscopy. *IEEE J Sel Top Quantum Electron*. In press.
- Hanley S, Arndt-Jovin DJ, Jovin TM. Spectrally resolved fluorescence lifetime imaging microscopy. *Appl Spectrosc* 56: 155–166, 2002.
- Harvey CD, Yasuda R, Zhong H, Svoboda K. The spread of Ras activity triggered by activation of a single dendritic spine. *Science* 321: 136–140, 2008.
- Helmchen F, Denk W. Deep tissue two-photon microscopy. *Nat Methods* 2: 932–940, 2005.
- Helmchen F, Kleinfeld D. In vivo measurements of blood flow, and glial cell function with two-photon laser scanning microscopy. *Methods Enzymol* 444: 231–254, 2008.
- Holtmaat A, Bonhoeffer T, Chow DK, Chuckowree J, De Paola V, Hofer SB, Hübener M, Keck T, Knott G, Lee WC, Mostany R, Mrsic-Flogel TD, Nedivi E, Portera-Cailliau C, Svoboda K, Trachtenberg JT, Wilbrecht L. Long-term, high-resolution imaging in the mouse neocortex through a chronic cranial window. *Nat Protocols* 4: 1128–1144, 2009.
- Ji N, Milkie DE, Betzig E. Adaptive optics via pupil segmentation for high-resolution imaging in biological tissues. *Nat Methods* 7: 141–147, 2010.
- König K, So PT, Mantulin WW, Tromberg BJ, Gratton E. Two-photon excited lifetime imaging of autofluorescence in cells during UVA and NIR photostress. *J Microsc* 183: 197–204, 1996.
- Ly S, McNeer G, Fore S, Chan J, Huser T. Time-gated single photon counting enables separation of CARS microscopy data from multiphoton-excited tissue autofluorescence. *Opt Express* 15: 16839–16851, 2007.
- Moreaux L, Sandre O, Blanchard-Desce M, Mertz J. Membrane imaging by simultaneous second-harmonic generation, and two-photon microscopy. *Opt Lett* 25: 320–322, 2000.
- Neher E, Hopt A. Highly nonlinear photodamage in the two-photon fluorescence microscopy. *Biophys J* 80: 2029–2036, 2001.
- Nguyen QT, Dolnick EM, Driscoll J, Kleinfeld D. MPScope 2.0: a computer system for two-photon laser scanning microscopy with concurrent plasma-mediated ablation and electrophysiology. In: *Methods for In Vivo Optical Imaging* (2nd ed.), edited by Frostig RD. Boca Raton, FL: CRC, 2009, p. 117–142.
- Nguyen QT, Tsai PS, Kleinfeld D. MPScope: a versatile software suite for multiphoton microscopy. *J Neurosci Methods* 156: 351–359, 2006.
- Nishimura N, Schaffer CB, Friedman B, Lyden PD, Kleinfeld D. Penetrating arterioles are a bottleneck in the perfusion of neocortex. *Proc Natl Acad Sci USA* 104: 365–370, 2007.
- Pepperkok R, Squire A, Geley S, Bastiaens PI. Simultaneous detection of multiple green fluorescent proteins in live cells by fluorescence lifetime imaging microscopy. *Curr Biol* 9: 269–272, 1999.
- Rueckel M, Mack-Bucher JA, Denk W. Adaptive wavefront correction in two-photon microscopy using coherence-gated wavefront sensing. *Proc Natl Acad Sci USA* 103: 17137–17142, 2006.
- Shaner NC, Steinbach PA, Tsien RY. A guide to choosing fluorescent proteins. *Nat Methods* 2: 905–909, 2005.

- Sheetz KE, Hoover EE, Carriles R, Kleinfeld D, Squier JA.** Advancing multifocal nonlinear microscopy: Development, and application of a novel multibeam Yb:KGd(W.O4)2 oscillator. *Opt Express* 16: 17574–17584, 2008.
- Shockley W, Pierce JR.** A theory of noise for electron multipliers. *Proc Inst Radio Eng* 26: 321–332, 1938.
- Squier J, Muller M, Brakenhoff GJ, Wilson K.** Third harmonic generation microscopy. *Opt Express* 3: 315–321, 1998.
- Steinkamp JA, Lehnert BE, Lehnert NM.** Discrimination of damaged/dead cells by propidium iodide uptake in immunofluorescently labeled populations analyzed by phase-sensitive flow cytometry. *J Immunol Methods* 226: 59–70, 1999.
- Suhling K, French PMW, Phillips D.** Time-resolved fluorescence microscopy. *Photochem Photobiol Sci* 4: 13–22, 2005.
- Svoboda K, Denk W, Kleinfeld D, Tank DW.** In vivo dendritic calcium dynamics in neocortical pyramidal neurons. *Nature* 385: 161–165, 1997.
- Tan YP, Llano I, Hopt A, Würriehausen F, Neher E.** Fast scanning and efficient photodetection in a simple two-photon microscope. *J Neurosci Methods* 15: 123–135, 1999.
- Tsai PS, Kleinfeld D.** In vivo two-photon laser scanning microscopy with concurrent plasma-mediated ablation: principles, and hardware realization. In: *Methods for In Vivo Optical Imaging* (2nd ed.), edited by Frostig RD. Boca Raton, FL: CRC, 2009, p. 59–115.
- Tsai PS, Migliori B, Campbell K, Kim T, Kam Z, Groisman A, Kleinfeld D.** Spherical aberration correction in nonlinear microscopy, and optical ablation using a transparent deformable membrane. *Appl Phys Lett* 91: 191102, 2007.
- Unal Cevik I, Dalkara T.** Intravenously administered propidium iodide labels necrotic cells in the intact mouse brain after injury. *Cell Death Differ* 10: 928–929, 2003.
- Vucinic´ D, Sejnowski TJ.** A compact multiphoton 3D imaging system for recording fast neuronal activity. *PLoS One* 2: e699, 2007.
- Wang XF, Kitajima S, Uchida T, Coleman DM, Minami S.** Time-resolved fluorescence microscopy using multichannel photon-counting. *Appl Spectrosc* 44: 25–30, 1990.
- Yasuda R, Harvey CD, Zhong H, Sobczyk A, van Aelst L, Svoboda K.** Supersensitive Ras activation in dendrites, and spines revealed by two-photon fluorescence lifetime imaging. *Nat Neurosci* 9: 283–291, 2006.
- Zworykin VK, Morton GA, Malter L.** The secondary emission multiplier. A new electronic device. *Proc Inst Radio Eng* 24: 351–375, 1936.

